Available online at www.sciencedirect.com
ScienceDirect
Continental Shelf Research 27 (2007) 1548–1567
CONTINENTAL SHELF RESEARCH
www.elsevier.com/locate/csr

A two-way nested coupled tide-surge model for the Taiwan Strait

Wen-Zhou Zhang[a], Hua-Sheng Hong[a,*], Shao-Ping Shang[a,b], De-Wen Chen[b], Fei Chai[c]

[a]*State Key Laboratory of Marine Environmental Science (Xiamen University), Xiamen, China*
[b]*Department of Oceanography, College of Oceanography and Environmental Sciences, Xiamen University, Xiamen, China*
[c]*School of Marine Sciences, University of Maine, Orono, USA*

Received 11 May 2006; received in revised form 13 January 2007; accepted 17 January 2007
Available online 4 February 2007

Abstract

A two-way nested coupled tide-surge prediction model was established and applied in the Taiwan Strait and adjacent sea area in this study. This two-dimensional (2D) model had a fine horizontal resolution and took into account the interaction between storm surges and astronomical tides, which made it suitable for depicting the complicated physical properties of storm surges in the Taiwan Strait. A two-way nesting technique and an open boundary condition developed from Flather's radiation condition and Røed and Smedstad's local mode idea, were successfully implemented in the model. A simulation experiment showed that the open boundary condition could be used in the coupled tide-surge model and that the performance of the two-way nested model was slightly superior in accuracy to that of the one-way nested one.

The fluctuations of storm surge residuals with tidal period at Sansha and Pingtan tide stations during the period of typhoon Dan in 1999 were well reproduced by the model, with the coupling effect between storm surges and tides indicating that the effect of astronomical tides upon typhoon surges should be considered in a storm-surge prediction model for the Taiwan Strait. The forecast experiment during typhoon Talim in 2005 showed that the storm surge prediction outputs by the model were better in the early 20 h of the forecast period of each model run than those in the later period due to the prediction accuracy of the typhoon track, maximum winds, and central air pressures.

Keywords: Coupled tide-surge model; Storm surge; Tide; Typhoon; Taiwan strait

1. Introduction

The Taiwan Strait, a long channel joining the East China Sea and the South China Sea, is located on the wide continental shelf of the China Sea (see Fig. 1). The strait is a shallow sea area with an average water depth of about 60 m (Ye et al., 1985). It is separated from the Western Pacific Ocean by Taiwan Island, which is situated on the edge of the continental shelf.

In the Taiwan Strait, complicated and sharp spatio-temporal variations are the main characteristics of the tide (Ye et al., 1985; Li et al., 2002). The tide is very strong and a semidiurnal tide dominates.

*Corresponding author. Tel.: +86 592 2182216; fax: +86 592 2095242.
E-mail address: hshong@xmu.edu.cn (H.-S. Hong).

0278-4343/$ - see front matter © 2007 Published by Elsevier Ltd.
doi:10.1016/j.csr.2007.01.018

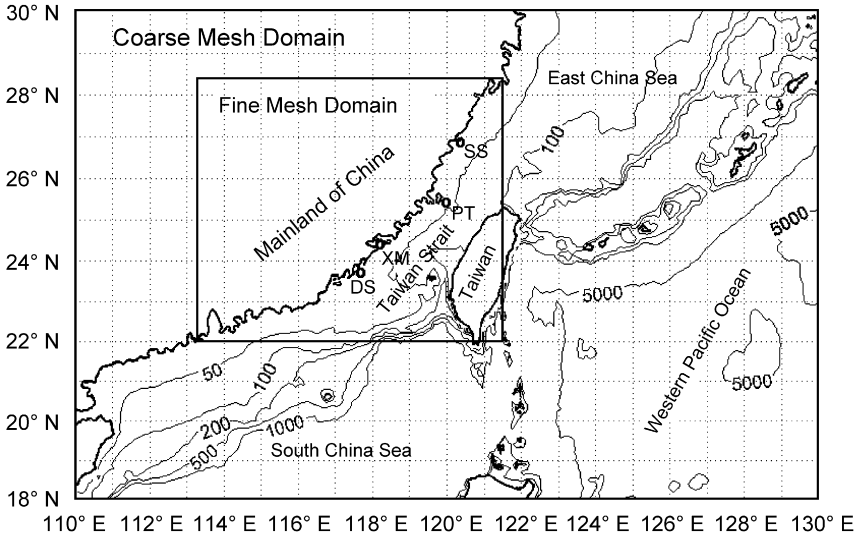

Fig. 1. Model domains for the coarse mesh and the fine mesh with bathymetric contours in meters. Sansha (SS), Pingtan (PT), Xiamen (XM) and Dongshan (DS) tide stations are marked by circles.

The tidal range along the western coast is larger than that along the eastern coast, and, as compared with that in the southern part, the range in the northern part is larger (Zhen et al., 1982; Fang et al., 1985; Li et al., 2002). The mean tidal ranges of some regions in the Taiwan Strait exceed 4 m, and the largest, 5.48 m, appeared at Bangmen in Sansha Bay (Fig. 2), in the northwestern part of the strait (Hu and Gu, 1989). The large monthly-mean ranges here often occur from August to October, coinciding with the typhoon season from June to October in the Taiwan Strait. According to previous studies, the interaction between tide and storm surge is notable where the water depth is small and the tidal range is large (Prandle and Wolf, 1978; Zhang and Wang, 1990; Pan and Liu, 1994). Consequently, it is believed that the interaction between tide and storm surge is significant in such a shallow sea area as the Taiwan Strait, in most regions of which the mean tidal ranges are quite large. Water level measurements during several typhoons at some gauge stations along the coast of Fujian Province, on the western bank of the Taiwan Strait, have confirmed this phenomenon (Zhang et al., 2004).

Storm surge numerical models have been developed for the Taiwan Strait by various investigators. Wu et al. (1982) set up a storm-surge model for the Taiwan Strait using vertically integrated equations, and made a nonlinear numerical computation on the storm surges caused by typhoon Vera in 1977. Although their model governing equations contained nonlinear advective terms, the effect of tide was not taken into account due to the lack of tide level values at the open boundary. Using this model, Wu (1984) enlarged the model area from the Taiwan Strait to the sea area to the southeast of China, but the model domain was still limited to the continental shelf of China and tide was not included. Chen et al. (1990) developed a 2D numerical model for predicting total water elevation in tidal rivers or bays with similar equations and applied it on the Minjiang River in Fujian Province (see Fig. 2). Here, tide was considered by superimposing tide level on the open boundary at the river mouth. Wang et al. (1991) established a typhoon surge model with a grid spacing of 13.89 km, in which the nonlinear advective terms of the vertically integrated equations were omitted and no tide was involved, and they divided the continental shelf sea area of China into five overlapping but unattached calculation domains. One of the five domains was located in the Taiwan Strait and adjacent area. These models were used in ocean engineering, storm surge investigation, or typhoon surge forecasting in the Taiwan Strait.

In light of the bathymetry and the tide characteristics described above, the storm surge prediction model for the Taiwan Strait should take into account the following two points: (1) the interaction between tide and surge in the whole area and (2)

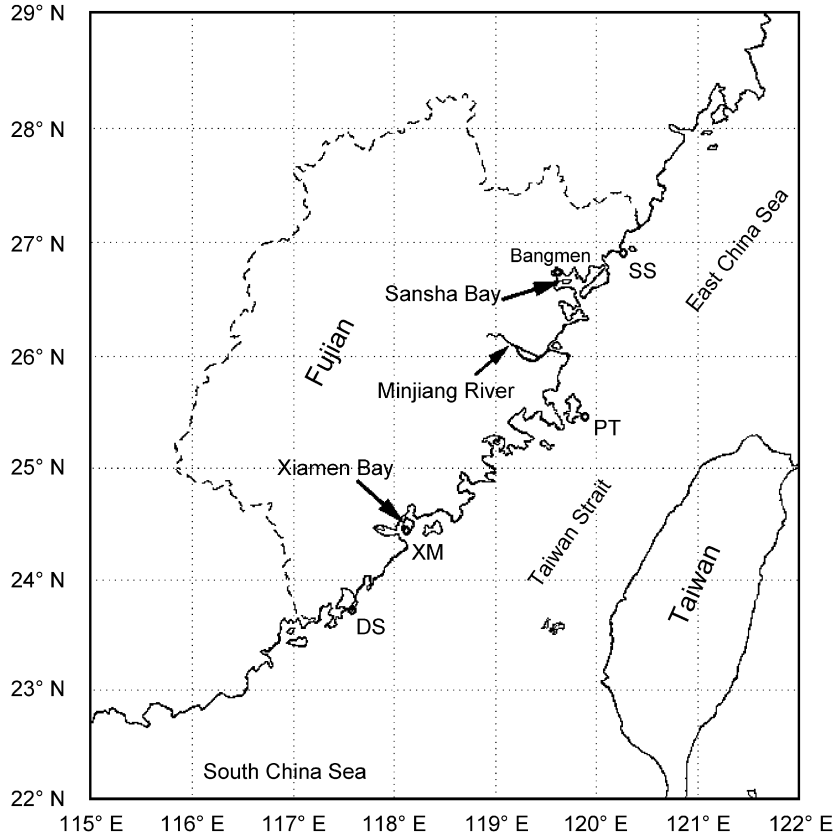

Fig. 2. Map of the Taiwan Strait (SS: Sansha station; PT: Pingtan station; XM: Xiamen station; DS: Dongshan station).

high horizontal resolution. In addition, it is also important to utilize a large enough model domain to ensure a lengthy forecast before a maximum tropical cyclone event occurs. However, none of the models mentioned above included these considerations. The main aim of this study was to develop a high-resolution coupled tide-surge prediction model for the Taiwan Strait using a two-way nesting technique.

2. Numerical model

The mathematical foundations of the two-way nested coupled tide-surge model (the NCTSM) are described in this section and the numerical scheme is shown in the Appendix A.

2.1. Basic equations

In the spherical coordinates, the following governing equations, including the depth-averaged continuity equation and momentum equations, were used in the present model.

$$\frac{\partial \zeta}{\partial t}+\frac{1}{R\cos\varphi}\left[\frac{\partial (Hu)}{\partial \lambda}+\frac{\partial (Hv\cos\varphi)}{\partial \varphi}\right]=0, \tag{1}$$

$$\begin{aligned}\frac{\partial u}{\partial t}+\frac{u}{R\cos\varphi}\frac{\partial u}{\partial \lambda}+\frac{v}{R}\frac{\partial u}{\partial \varphi}-\frac{uv\tan\varphi}{R}-fv \\ =-\frac{g}{R\cos\varphi}\frac{\partial \zeta}{\partial \lambda}-\frac{1}{\rho R\cos\varphi}\frac{\partial p_a}{\partial \lambda} \\ +\frac{1}{\rho H}(F_s-F_b),\end{aligned} \tag{2}$$

$$\begin{aligned}\frac{\partial v}{\partial t}+\frac{u}{R\cos\varphi}\frac{\partial v}{\partial \lambda}+\frac{v}{R}\frac{\partial v}{\partial \varphi}+\frac{u^2\tan\varphi}{R}+fu \\ =-\frac{g}{R}\frac{\partial \zeta}{\partial \varphi}-\frac{1}{\rho R}\frac{\partial p_a}{\partial \varphi}+\frac{1}{\rho H}(G_s-G_b),\end{aligned} \tag{3}$$

where t is the time; λ, φ the east longitude and north latitude; ζ the sea surface elevation above the undisturbed sea level; h the depth of undisturbed water; H the total water depth, $H=h+\zeta$; u, v the east and north components of the depth-mean

current, $\mathbf{q}$; F_s, G_s the components of the wind stress on the sea surface, $\boldsymbol{\tau}_s$; F_b, G_b the components of the bottom stress, $\boldsymbol{\tau}_b$; p_a the atmospheric pressure on the sea surface; R the radius of the earth; g the acceleration due to gravity; f the Coriolis parameter, $f = 2\omega \sin\varphi$, here ω is the angular speed of the earth's rotation; $\boldsymbol{\rho}$ the density of seawater, assumed to be unchanged.

The origin of the system of coordinates is located on the undisturbed sea surface. ζ is representative of vertical displacement of the sea surface from its undisturbed position (above which it is positive and below which it is negative), and it denotes tide level, storm surge, or their combination (namely total sea level). Storm surge or residual elevation is customarily defined as the difference between the total sea level and the predicted astronomical tide level.

Because bottom stress is the only energy-dissipating term in the above governing equations, it is significant in computing the tide and surge motions. Its dependence on current is well known and the quadratic law has been broadly used in the bottom friction parameterization. In recent years, the influence of wind wave and wave–current interaction upon bottom stress has been investigated, using numerical models (Zhang and Li, 1997; Jones and Davies, 1998, 2001). In shallow coastal regions, the levels of turbulence are enhanced by wind wave orbital velocity at the sea bed, while in deeper sea areas this effect is of less importance (Zhang and Li, 1997; Jones and Davies, 1998, 2001; Davies et al., 2000). This indicates that the magnitude of bottom stress in the shallow sea is larger than that in the deep sea due to wind wave effect. Zhang and Li (1997) remarked that this process could be parameterized by changing the bottom drag coefficient in a three-dimensional (3D) model to allow for wind wave effects. It was stated by Bao et al. (2001) that the bottom drag coefficient should be non-uniform and depth-dependent in the quadratic friction form in their 3D tide model. As is known, the velocity related to the bottom stress in the quadratic friction formulation is usually referred to the flow of the bottom boundary layer. However, a 2D model can also take into account the wave–current interaction with the appropriate parameterization and make storm surge predictions of a comparable accuracy with a 3D model (Jones and Davies, 1998). Since the model domain covers both shallow water and the deep sea, non-uniformity of the bottom drag coefficient might be required, although only depth-average current is considered in a 2D model (Kang et al., 1998). The depth of water in the calculation domain varies from less than 5 m to more than 7000 m. Consequently the depth-dependent bottom friction by means of a depth-dependent drag coefficient could be expected. The following formula relates the bottom stress to the depth-mean current, $\mathbf{q}$, using a quadratic law:

$$\boldsymbol{\tau}_b = \rho g c^{-2} |\mathbf{q}| \mathbf{q}, \tag{4}$$

where c is the Chezy coefficient, $c = H^{1/6}/n$, n denoting the Manning coefficient. The bottom friction formulation (4) is also implied in a 2D tide model by Kang et al. (1998) and in a 2D storm-surge model by Zhang and Li (1996).

In low-lying coastal regions, dry places may be flooded with increasing water level and in very shallow near-shore regions, wet areas may be dried out with decreasing water level. A wetting and drying scheme has been applied in some models to include this effect (e.g. Flather, 1994; Jones and Davies, 1998, 2001). Because the horizontal resolution (1/30°, about 3.7 km) of NCTSM is not fine enough to effectively handle this process in the area of interest, wetting or drying of the grid is not considered here. In order to prevent wet points from drying out, the water depth of a few points shallower than 4.5 m is artificially set to 4.5 m since the measured maximum tidal range is less than 9 m in this area (Hu and Gu, 1989). Since inundation caused by typhoon surges is very dangerous in some low-lying coastal areas, some finer grid domains should be nested into this model in the future, in order to take account of the wetting and drying effect.

The parameterization of the wind stress is also completed with a quadratic law as follows:

$$\boldsymbol{\tau}_s = \rho_a C_d |\mathbf{W}| \mathbf{W}, \tag{5}$$

where C_d is the wind-stress coefficient (drag coefficient), ρ_a the density of air, and $\mathbf{W}$ the wind vector at a height of 10 m above sea surface. Based on several investigations (Garratt, 1977; Smith, 1980; Large and Pond, 1981; Wu, 1982; Geernaert et al., 1987; Yelland and Taylor, 1996; Powell et al., 2003), C_d in this paper was determined from the equation:

$$C_d \times 10^3 = \begin{cases} 1.052, & |\mathbf{W}| \leqslant 6\ \mathrm{m/s}, \\ 0.638 + 0.069|\mathbf{W}|, & 6 < |\mathbf{W}| < 30\ \mathrm{m/s}, \\ 2.708, & |\mathbf{W}| \geqslant 30\ \mathrm{m/s}. \end{cases} \tag{6}$$

In order to make Eqs. (1)–(3) closed, initial and boundary conditions must be specified. The effect of initial conditions on the calculated results over several days almost disappears in the model, and therefore the initial conditions were set to zero, known as "cold start".

$$\zeta = u = v = 0, \quad \text{at time } t = 0. \tag{7}$$

Along the coastal boundaries, no water is allowed to flow through, which means that the normal component of the current vanishes. On the open boundaries, a radiation condition following Flather (1976) was used to prevent the artificial reflection at the open boundaries of disturbances generated within the model area,

$$q_n = \hat{q}_n \pm \frac{C}{H}\left(\zeta - \hat{\zeta}\right), \tag{8}$$

$$\hat{q}_n = q_n^T + q_n^M,$$

$$\hat{\zeta} = \zeta^T + \zeta^M,$$

where the subscript n stands for the component normal to the open boundary; the superscripts, M and T, denote the contributions to the total water elevation or the current component, associated with the meteorological force and the tide input, respectively; and $C = (gH)^{1/2}$. ζ^T and ζ^M are given by the forms:

$$\zeta^T = \sum_{i=1}^{m} f_i H_i \cos(\sigma_i t + V_i + u_i - g_i), \tag{9}$$

$$\zeta^M = \frac{p_e - p_a}{\rho g}, \tag{10}$$

where H_i and g_i are the harmonic constants, amplitude and phase-lag of the ith tidal constituent, respectively, σ_i the angular speed, f_i the nodal factor, u_i the nodal angle, and V_i the initial phase angle of the equilibrium constituent at Greenwich. p_e (Pa), month-dependent, is the ambient pressure or environmental pressure and can be specified beforehand. The harmonic constants of eight principal tidal constituents (M_2, S_2, N_2, K_2, K_1, O_1, P_1 and Q_1) used in the present model on the open boundary could be obtained from the global tide model (Matsumoto et al., 2000), and σ_i, f_i, u_i and V_i are defined in advance. It is unrealistic to accurately give ${q_n}^M$ and ${q_n}^T$ ahead of time. For that reason, the sum of ${q_n}^M$ and ${q_n}^T$, $\hat{q}_n$, was determined by the method put forward by Røed and Smedstad (1984), the so-called "local" solution, where both the meteorological forces and the bottom friction are taken into account. At the same time, the current component tangential to the open boundary was calculated directly by this method. For example, those at the eastern open boundary could be calculated by the equations:

$$\frac{\partial u}{\partial t} = \frac{uv \tan\varphi}{R} + fv + \frac{1}{\rho H}(F_s - F_b), \tag{11}$$

$$\frac{\partial v}{\partial t} = -\frac{u^2 \tan\varphi}{R} - fu - \frac{g}{R}\frac{\partial \zeta}{\partial \varphi} - \frac{1}{\rho R}\frac{\partial p_a}{\partial \varphi} + \frac{1}{\rho H}(G_s - G_b), \tag{12}$$

$$\frac{\partial \zeta}{\partial t} = -\frac{1}{R\cos\varphi}\frac{\partial (Hv\cos\varphi)}{\partial \varphi}. \tag{13}$$

This open boundary condition is slightly different from the scheme (FRO, a modification to Flather's radiation condition) proposed by Palma and Matano (1998). In this scheme, the water level ($\hat{\zeta}$) at the open boundary was specified and the normal component ($\hat{q}_n$) of current was the local mode or the local solution, following Røed and Smedstad (1984), which only contained the contribution due to local forces, e.g. the wind stress and the bottom stress. As we know, both current and water level at the open boundary are local solutions in the FRO (Palma and Matano, 1998).

2.2. Two-way nesting

There is an economical way to improve the horizontal resolution of a numerical forecast model by nesting a fine mesh within a coarse mesh, since the nested model could save computer time and memory space compared with a model having the same fine resolution throughout the whole model domain (Koch and McQueen, 1987). The grid nesting could be implemented by one of two means: one-way and two-way nesting. In a one-way nested grid model, information from the coarse mesh could enter and affect the fine mesh through the interface between them, while disturbances from the fine mesh do not feed back to the coarse. In other words, the coarse model is entirely independent of the fine model. Because it is simpler and requires less computer time (Koch and McQueen, 1987; Yu and Zhang, 2002), this approach is used in most nested ocean and atmosphere models (e.g. Davies and Flather, 1978; Roy, 1995; Kunz and Moussiopoulos, 1997; Ådlandsvik and Hansen, 1998;

Monbaliu et al., 2000; Yu and Zhang, 2002). In a two-way nested grid model, however, not only does the coarse grid model affect the fine grid model, but the fine also influences the coarse. Koch and McQueen (1987) remarked that the exchange of information between the two grid meshes was more realistic particularly when strong mesoscale disturbances were generated within the fine model; therefore, the two-way interactive nested grid method was intuitively the more appealing of the two approaches. Thus, a two-way nesting technique was applied to the present model in order to improve the storm surge predictions, even though more programming effort and computer time were necessary.

The domains of the coarse mesh (110–130°E, 18–30°N) and the fine mesh (113.3–121.5°E, 22.0–28.4°N) are shown in Fig. 1, and the coarse mesh mantled the whole fine mesh. The offshore islands, which can be distinguished by model grids, were incorporated in the model. The sea area southeast of Taiwan Island was not included in the practical computation of the fine grid, which can save some computer time, since the computed results for the fine mesh there do not affect the target area, the Taiwan Strait. The ratio of the coarse grid size, 1/10° (about 11.1 km), to the fine grid size, 1/30° (about 3.7 km), is an integer, 3, and the time-steps of the two models are a consistent value (400 s in this study), avoiding the additional error caused by temporal interpolation at the open boundary of the fine mesh region. They are based on the uniform governing equations and initial conditions described above.

The interface conditions, typically including the open boundary conditions of the fine mesh and the feedback method for the coarse mesh (Koch and McQueen, 1987), are of great importance for the two-way nested model in maintaining stability and reducing errors. For the same purpose mentioned previously, the open boundary conditions of the fine mesh field are also given by Eq. (8). $\hat{q}_n$ was obtained from the mass flux at the open boundary, interpolated from that of the coarse grid through the cubic spline interpolation method, and so was the tangential component of the current, since it can satisfy the one-dimensional form of the continuity Eq. (1) and thus, to some extent, keeps the conservation of mass. After the calculations in the fine mesh were completed, the average of the water elevations of all fine grid cells within a coarse cell district—except for the points at the interface boundaries—replaced the water elevation of the coarse cell as a new value in the common region. To summarize, in one time-step, the nested model first performed the computations with the open boundary conditions in the coarse grid domain, then drove the fine mesh to compute through the interface conditions, and finally fed back the information from the fine mesh to the coarse mesh.

2.3. Cyclone model

Meteorological driving forces of storm surges consist of wind stress and atmospheric pressure gradient. Therefore, determining the wind field and pressure field of a tropical cyclone is significant and indispensable for cyclone surge calculations.

An asymmetric wind field model for a moving cyclone was developed by Jelesnianski (1965) and is widely used in many tropical cyclone surge models (e.g. Wu, 1984; Sun et al., 1994; Roy, 1995). It was adopted in this paper and is described as follows:

$$\mathbf{W} = \frac{r}{r_m + r}(U\mathbf{i} + V\mathbf{j}) + W_m \frac{1}{r}\left(\frac{r}{r_m}\right)^{3/2}(a\mathbf{i} + b\mathbf{j}), \quad 0 < r \leqslant r_m,$$

$$\mathbf{W} = \frac{r_m}{r_m + r}(U\mathbf{i} + V\mathbf{j}) + W_m \frac{1}{r}\left(\frac{r_m}{r}\right)^{1/2}(a\mathbf{i} + b\mathbf{j}), \quad r > r_m, \tag{14}$$

$$a = -(r_\lambda \sin\theta + r_\varphi \cos\theta),$$

$$b = r_\lambda \cos\theta - r_\varphi \sin\theta,$$

where $(\mathbf{i}, \mathbf{j})$ are unit vectors in longitude and latitude, U, V the components of the translation velocity of the cyclone center, r_m the radius to maximum wind speed W_m, r the radial distance from the cyclone center, r_λ and r_φ the components of the vector $\mathbf{r}$, and θ inflow angle of range 0–30°.

The atmospheric pressure field for the cyclone was calculated using the following formula (Holland, 1980; Jakobsen and Madsen, 2004):

$$p_a = p_c + \Delta p \exp\left[-\left(\frac{r}{r_m}\right)^{-B}\right], \quad \Delta p = p_e - p_c, \quad r > 0, \tag{15}$$

where p_c (Pa) is the central pressure of the cyclone and Δp the pressure drop or the pressure deficit; B is the shape parameter, which can be estimated by the following empirical relationship for the western North Pacific (Atkinson and Holliday, 1977;

Jakobsen and Madsen, 2004)

$$B = 0.1397(\Delta p)^{0.288}. \quad (16)$$

When r equals zero, p_a is set to p_c and $\mathbf{W}$ is set to zero.

3. Hindcast simulation and forecast experiment

3.1. Calculation scheme

The present model can be used to calculate tide only; pure storm surge, which is without the effect of tide; or tide plus surge motion by the control of tidal input at the open boundary of the outer domain and meteorological forcing. For the sake of the storm surge with the coupling effect of tide and surge, the model should be run twice: once to simulate the total water level (tide plus surge) with tidal input and meteorological forcing; and again to predict the tide only, without meteorological forcing. The storm surge elevation time series was gained by subtracting the tide level from the corresponding total water level.

It took about 3 days for the tide computation in this model to remove the influence of zero initial conditions on the calculation results. Thus, in computing the total water level, the model simulated tide only for 3 days before introducing meteorological forces, which means that the initial conditions of coupled tide-surge computation were actually the water level field and depth-mean current field of the astronomical tide.

The wind speed was multiplied by a relaxation coefficient, which changes from 0 to 1, during the first 100 time-steps, about 11.1 h after the start-up of meteorological forces. This reduces the impact on calculations if strong winds blow suddenly. A similar method was applied also to the water elevation on the open boundary of the coarse mesh model. This approach was very effective in avoiding artificial disturbances just after an external force was introduced into the model.

The computed values of every selected wet grid point nearest to a tide gauge site were used for comparison with the observations at the corresponding tide station. Of course, there was some difference in space between the selected grid point and the corresponding station, and this introduced some errors. However, the distance between them was no more than $2^{-1/2}\Delta s$ (Δs being the maximum grid spacing), and for the fine resolution grid mesh the errors due to this difference were negligible. The water level observations, obtained with float-type tide gauges, at the four tidal gauge stations (shown in Fig. 2), managed by the State Oceanic Administration of China were used to validate the output of results by the model. The observation errors of these data were not more than ± 1 cm.

3.2. Tide computation

Tide plays an important role in the interaction between tide and storm surge (Prandle and Wolf, 1978). Therefore, it was crucial to verify the computations of tides using the present model.

Water level is affected by meteorological forces, especially by strong winds in the shallow sea area. In order to reduce the effect of winds on water level, there should be no wind or as weak a wind as possible in the days selected for the validation of tide computations. The weather was calm with wind speeds lower than 9 m/s in nearly 94% of the total time at Pingtan station, and lower than 7 m/s in over 96% of the time at Xiamen station during the period from 0000 LST 5 August to 2300 LST 20 August 2000 (LST refers to local or Beijing standard time, which is 8 h ahead of the corresponding UTC, and will be used in this paper). The exception arose from the small effect of the outermost portion of typhoon Jelawat, which passed through the sea area to the north of the Taiwan Strait, during 9–11 August 2000. Using NCTSM, we computed the tides only, covering the period from 2 to 20 August 2000.

Fig. 3 shows the results of the computation omitting the first 3 days due to zero initial conditions. As seen in Fig. 3, the results clearly reproduce the variations of tides at Sansha, Pingtan, Xiamen and Dongshan. For purposes of analysis, the computed time series of tide levels with an interval equaling the time step of the model was linearly interpolated to the corresponding hourly data, because the observations were made hourly. The mean absolute errors (MAE) between the computed values and the observations were under 15 cm, and the standard deviations of errors (STDE) did not exceed 18 cm (Table 1). The correlation coefficients (R) are shown in Table 1 with a corresponding statistical significance of 99%. It can be seen from Fig. 4 that the residuals of tide computations still contained tidal components. Their amplitudes and characteristics depended on the place and the period. For example, the

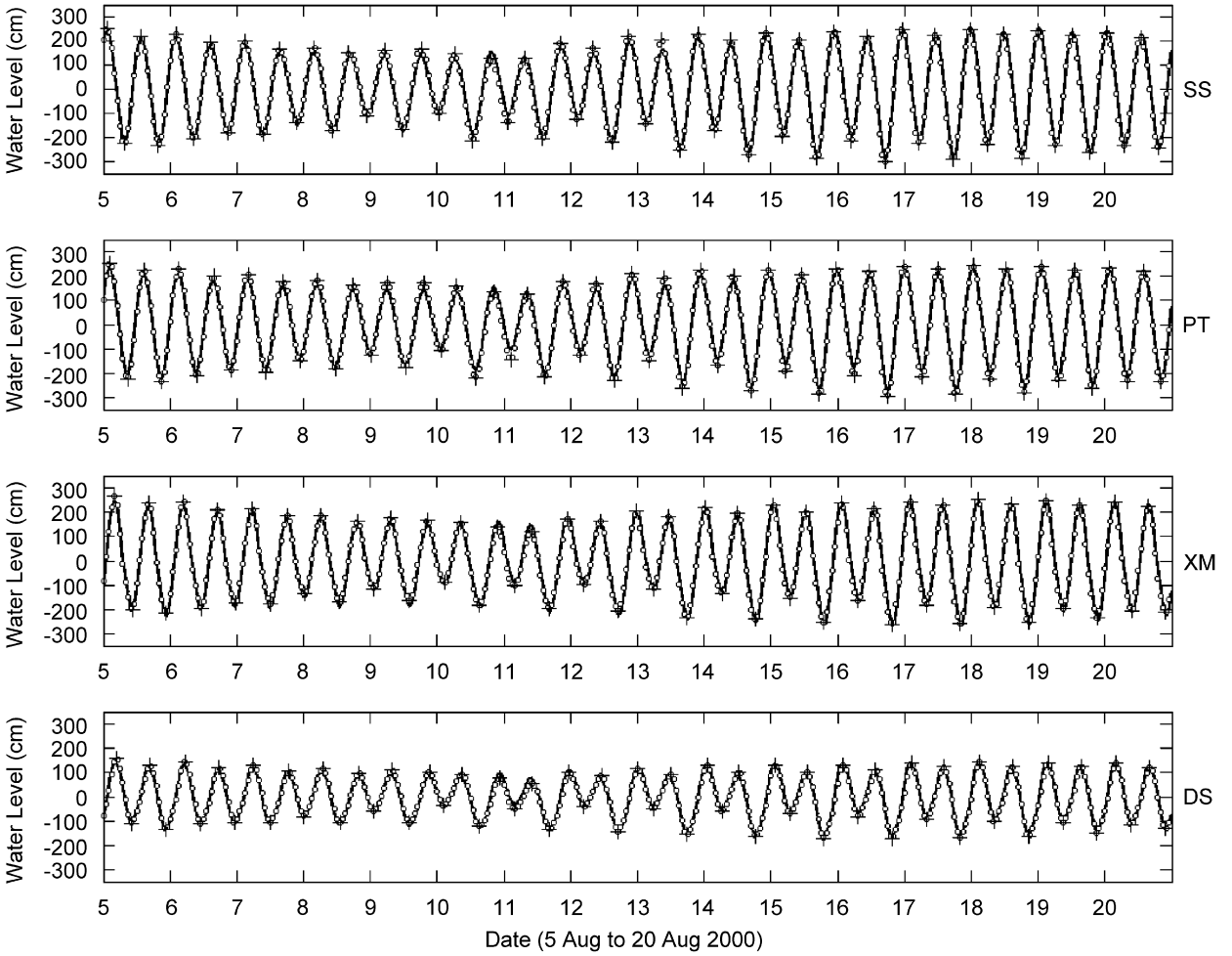

Fig. 3. Time series of water levels (referred to the mean sea level during the period) at the four tide stations (continuous lines: numerical results, circles: hourly observations, plus signs: observed high tides or low tides).

Table 1
Comparisons of the MAE (cm), STDE (cm) and R between numerically computed tides and harmonically-calculated tides

Stations	Numerically-computed tides			Harmonically-calculated tides		
	MAE	STDE	R	MAE	STDE	R
Sansha	12.5	15.2	0.995	9.1	12.0	0.997
Pingtan	14.3	17.3	0.996	10.3	13.0	0.997
Xiamen	13.2	16.0	0.994	10.1	12.6	0.996
Dongshan	11.8	14.7	0.984	8.2	9.8	0.993
mean	12.95	15.80	0.992	9.43	11.85	0.996

amplitudes during the period from 5 to 8 August were obviously larger than those during the period from 18 to 20 August at Pingtan station, and just the reverse at Sansha and Xiamen stations. A semidiurnal component was dominant in the residuals at Pingtan, which was mainly due to the marked computation errors of the M_2 constituent (Table 2). The shallow water effect played an important role in the residuals, which included visible higher-frequency fluctuations than the M_2 constituent at Xiamen station, since this station was located in Xiamen Bay.

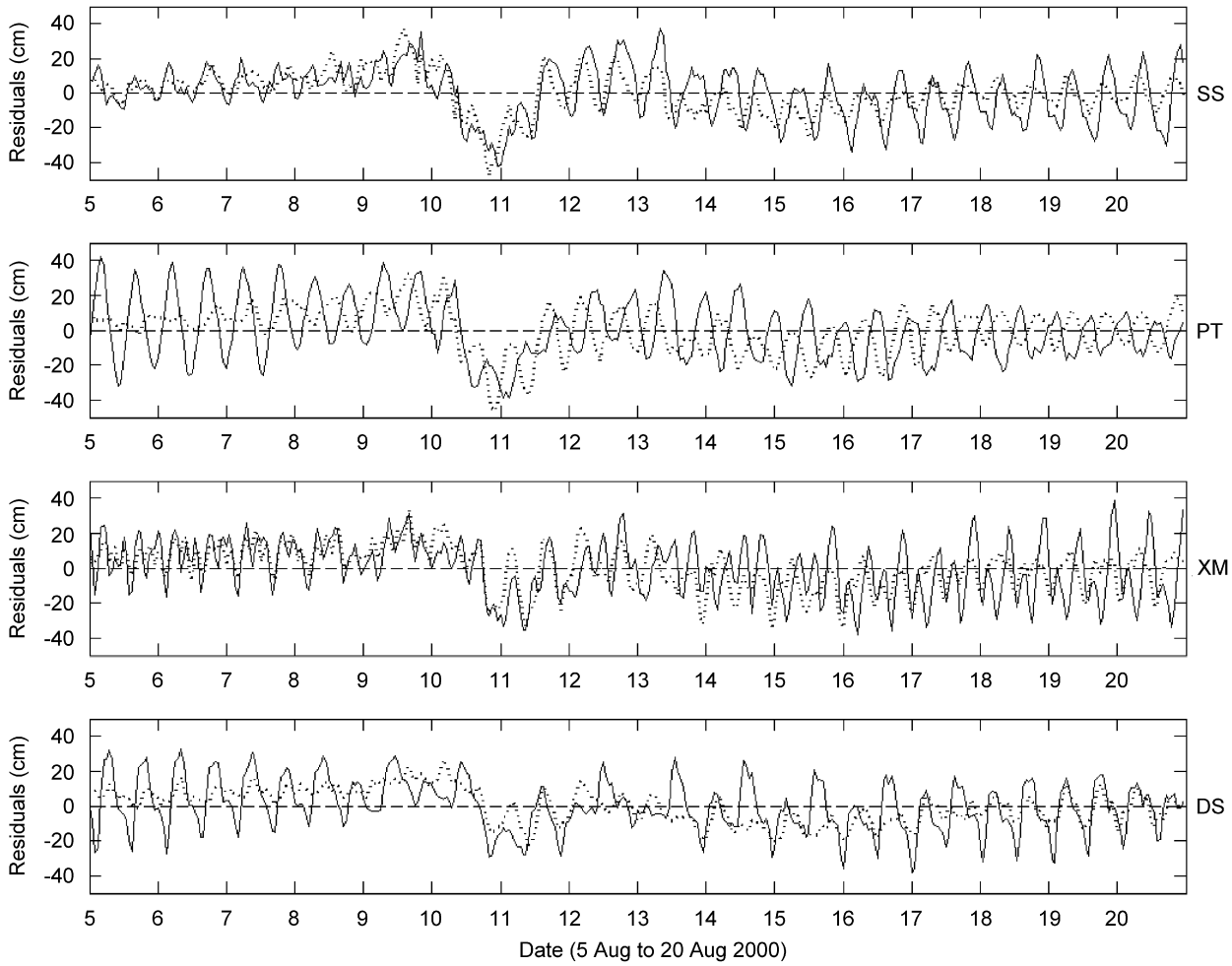

Fig. 4. Residual (observations minus calculations) series of tide levels calculated by NCTSM (continuous line) and by the harmonic method (dotted line).

Table 2
The differences (simulated minus measured) in amplitude (cm) and in phase-lag (deg.) between simulated and measured harmonic constants of four principal constituents

Stations	M_2		S_2		K_1		O_1	
	ΔH_i	Δg_i	ΔH_i	Δg_i	ΔH_i	Δg_i	ΔH_i	Δg_i
Sansha	−4	2	3	9	0	2	3	2
Pingtan	−15	−3	0	2	0	−2	3	−3
Xiamen	4	2	3	5	3	−3	5	−1
Dongshan	−1	−8	1	−7	2	−9	4	−6

On the other hand, the computed high tide levels during the period from the afternoon of 10 August to the morning of 11 August obviously exceeded the observations (see Figs. 3–5), which was due mainly to the negative set-ups caused by the winds in the left portion of typhoon Jelawat mentioned above.

In order to ultimately show the performance of the model computing tide, the above simulated and observed hourly data were harmonically analyzed, using the least-squares fit method. According to the Rayleigh criterion, only four principal constituents (M_2, S_2, K_1 and O_1) should be included in the analysis with the recording length of 384 h during 16 days mentioned previously (Foreman, 1977). Table 2 shows the differences in amplitude and phase-lag between the constants from simulated results and those from observations. It can be seen that the absolute values of the differences in amplitude did not exceed 5 cm except at the Pingtan station, and the absolute errors of phase-lags were not more than 10°, suggesting that, on the part of the four principal constituents, the simulated results were in good agreement with the observed.

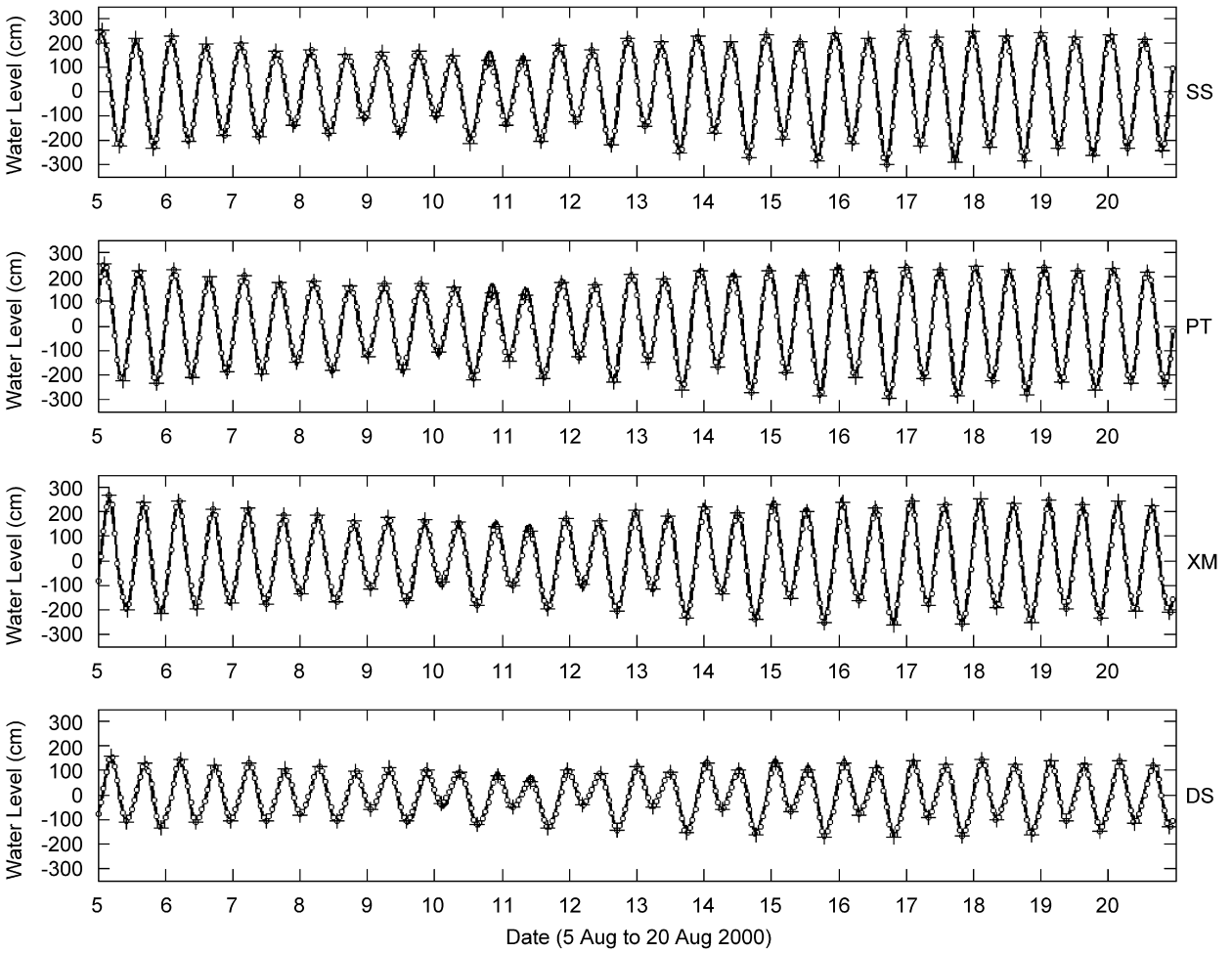

Fig. 5. Time series of water levels (referred to the mean sea level during the period) at the four tide stations (continuous lines: harmonically calculated results, circles: hourly observations, plus signs: observed high tides or low tides).

In this paper the accuracy of numerically computed tides via NCTSM was still no better than that of harmonically calculated tides with 170 constituents. The astronomical tides calculated using the harmonic method for the same period as above were nearly consistent with the measurements (Fig. 5). The varying amplitudes of calculation errors by this method were commonly smaller than those by the numerical model (Fig. 4). Seen from Table 1, the values of both MAE and STDE from harmonically computed data series were also smaller than their counterparts from numerically calculated results, and the correlation between harmonically calculated tides and the observations was better based on their *R*-values. That is why the observed storm surge elevations were derived by subtracting the harmonically calculated tide levels, rather than the numerically computed ones, from the observed water levels. For the same reason, the storm surges computed in the present model were defined as the differences between the tide levels from the tide run and the corresponding total water levels from the tide-surge coupling run, in order to eliminate additional errors due to inaccurate tide computations by the model, compared with those by the harmonic method. Since harmonically predicted astronomical tide levels are generally more accurate than numerically predicted ones, it still may be an optimal choice that total water-level predictions used for hazard mitigation are obtained from the results of numerically predicted storm surges plus harmonically predicted astronomical tides (Flather, 2000).

Although the accuracy of the tides computed by NCTSM was no higher than that by the harmonic method used in this paper, it is credible enough to

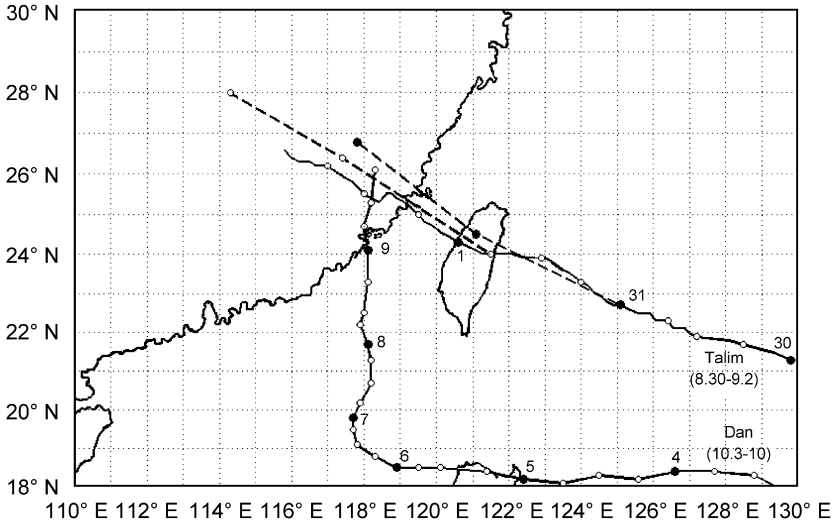

Fig. 6. Tracks of typhoons Dan and Talim. Continuous line shows the best track (Dan) or the analyzed track (Talim). Black dots denote the typhoon positions at 0800 LST on the dates labeled by corresponding numbers, circles denote typhoon positions at 0200, 1400 or 2000 LST, and broken lines show forecasted tracks in the following 24 and 48 h.

take into account the coupling effect of tides and storm surges in computing typhoon surges.

3.3. Hindcast simulation

The model was used to simulate the storm surges caused by typhoon Dan during October 1999. The track of typhoon Dan is shown in Fig. 6, based on the best track data published by the China Meteorological Administration (CMA). Dan developed from a tropical depression and reached typhoon strength late on 4 October in the northern West Pacific. After moving west for about 2 days, it abruptly turned north late on 6 October and continued moving north until it landed near Xiamen, in Fujian Province at 1000 LST 9 October, with a maximum wind speed of 35 m/s and a central pressure of 970 hPa.

Using typhoon data, including the typhoon's position, maximum wind speed, and central pressure data obtained from CMA, a model hindcast simulation, covering the period from 0800 LST 3 October to 0800 LST 10 October, was carried out according to the scheme mentioned above. In addition, and for comparison, another pure storm surge simulation was also done.

Fig. 7 shows the time series of the simulated, the measured, and the pure storm surges at the locations indicated in Fig. 1. It is easy to see that the simulated typhoon surge elevations, with the effect of tide and surge interacting, were consistent with the measurements, and obviously better than the pure typhoon surges. This indicated that the fluctuation of storm surge residuals with tidal period was attributable to the interaction between tide and storm surge (Fig. 7a,b). Therefore, these fluctuations of the storm surges in the northern part of the Taiwan Strait could not be ascribed simply to the harmonically forecasting errors of astronomical tides, but were principally due to the interaction between tide and storm surge. The largest difference between the surge elevation with the coupling effect and the pure surge elevation exceeded 24 cm at every station in Fig. 7, demonstrating that the interaction was considerable in this sea area.

Fig. 6 shows that typhoon Dan moved more or less along the open south boundary of the larger model domain before turning north, which was a good test for the model, especially for its open boundary conditions. The good performance of the hindcast simulation indicated to some extent that the open boundary conditions used in the model were reasonable and dependable.

To show the effect of the two-way nesting on storm surge computation, another model run with one-way nesting, namely no feedback for the coarse grid model, was conducted. From Table 3, we can see that on average, the error decreased 0.27 cm for the fine grid model and 0.52 cm for the coarse grid model, and the STDE were reduced 0.25 and 0.55 cm, respectively, when the two-way nesting was compared with the one-way nesting. The

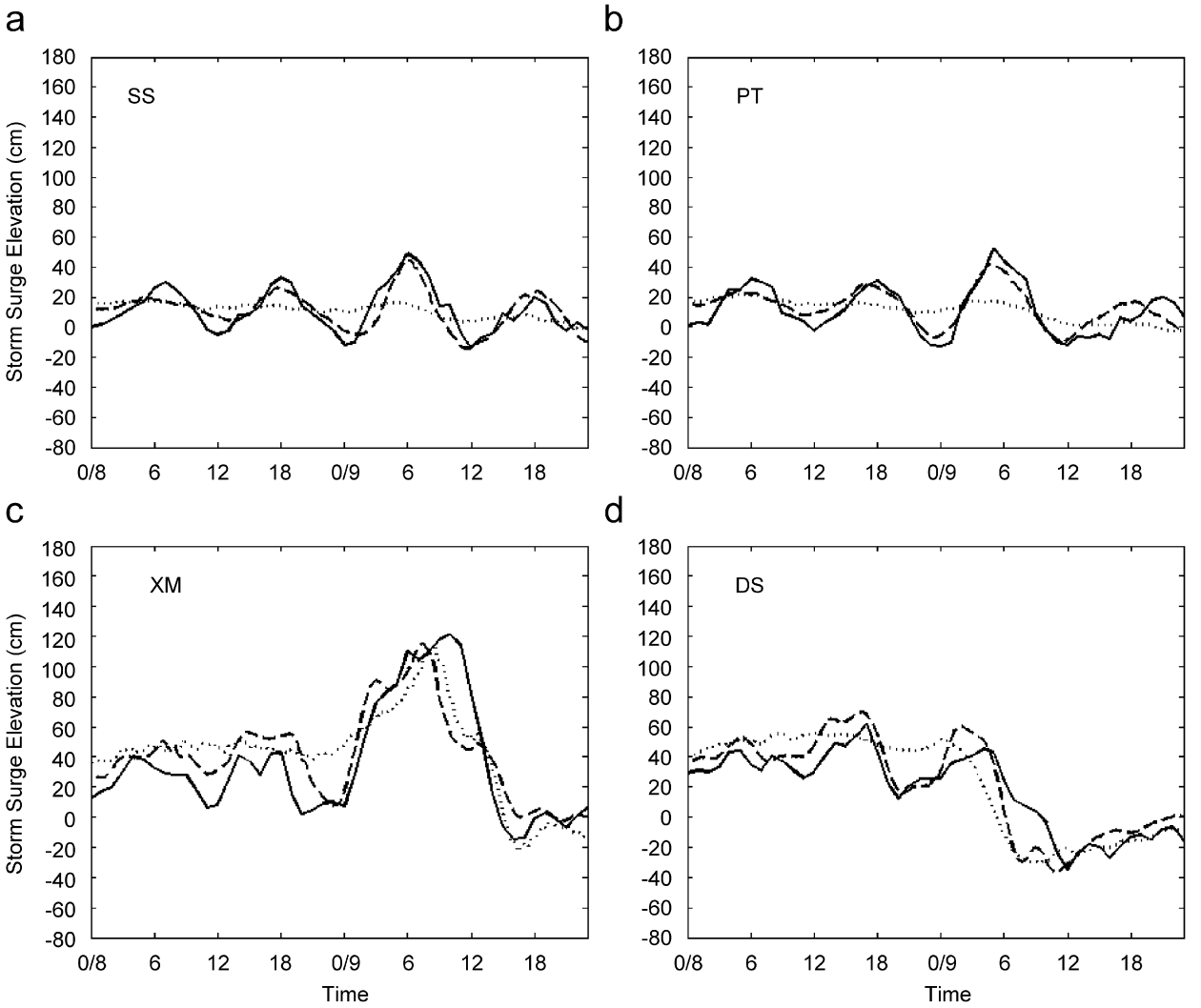

Fig. 7. Time series of measured storm surge (continuous line), simulated storm surge (broken line) and calculated pure storm surge (dotted line) for the period from 0000 LST 8 October to 2300 LST 9 October 1999.

Table 3
The MAE (cm)/STDE (cm)/*R*-values of simulated storm surges for typhoon Dan

Stations	One-way nesting		Two-way nesting	
	Fine grid	Coarse grid	Fine grid	Coarse grid
Sansha	7.1/8.3/0.827	7.7/9.5/0.770	6.9/8.1/0.836	7.0/8.2/0.833
Pingtan	7.8/9.1/0.832	7.9/9.4/0.829	7.4/8.7/0.851	7.7/9.1/0.850
Xiamen	16.1/21.2/0.834	17.3/20.0/0.852	16.0/21.2/0.835	16.9/21.2/0.834
Dongshan	11.8/14.2/0.903	12.3/15.4/0.896	11.4/13.8/0.907	11.5/13.6/0.911
mean	10.70/13.20/0.849	11.30/13.58/0.837	10.43/12.95/0.857	10.78/13.03/0.857

R-value with a statistical significance of 99% by two-way nesting was a little higher than that by one-way nesting (see Table 3). This showed that the one-way nested model was comparable in accuracy with the two-way nested model, based on both MAE and STDE. As shown in Table 4, the

Table 4
The differences (cm, simulated minus measured) in the maximal hourly typhoon surge elevations between the simulated and the measured data for typhoon Dan

Stations	One-way nesting		Two-way nesting	
	Fine grid	Coarse grid	Fine grid	Coarse grid
Sansha	−6.0	−8.0	−4.2	−4.7
Pingtan	−11.6	−18.6	−11.0	−17.7
Xiamen	−8.1	13.5	−7.3	−6.2
Dongshan	7.8	7.1	7.2	7.3

differences between the simulated and the observed maximal surge elevations, based on hourly data, were reduced by applying the two-way nesting technique. The largest reduced magnitude was 1.8 cm for the fine grid at the Sansha station and 7.3 cm for the coarse grid at the Xiamen station. Tables 3 and 4 demonstrate that both the fine grid model and the coarse grid model were slightly improved by two-way nesting, and more improvement was made in the coarse model than in the fine one. In addition, it is easy to see that the results from the fine model were usually better than those from the coarse model, indicating that the nesting technique, whether one-way nesting or two-way nesting, could really improve the performance of the numerical model. Since the one-way nested model required less computer time and was comparable with the two-way nested model in accuracy based on the above comparisons, it is acceptable to use the one-way nested model from the operational point of view.

3.4. Forecast experiment

To examine the forecasting capability of the model, a model forecast experiment was carried out in real time during typhoon Talim, covering the period from 0800 LST 29 August to 0200 LST 2 September 2005. The analyzed track in real time and the forecasted track, based on the data from CMA, are shown in Fig. 6. Generally speaking, the interval of the analyzed data from CMA was 6 or 3 h, depending on the strength of the tropical cyclone and the distance from China, and was even shortened to 1 h when the cyclone was expected to heavily affect the coasts of China. The forecasted data of cyclone tracks for the coming 24 and 48 h is usually published every 6 h, at 0200, 0800, 1400 or 2000 LST every day. Thus, the track of Talim was updated with the input of new analyzed and forecasted data each time the model was run.

During the period from 0800 LST 31 August to 1700 LST 1 September 2005, the model was run every 3 or 6 h depending on the interval of the track data, and lasted less than 30 min each time. The two time series of forecasted storm surge residuals after the corresponding start time are shown in Figs. 8 and 9, respectively, and by comparison, the observations and the hindcast simulation results based on the "best track" (not formally published at present) data are showed, too.

Fig. 8 shows that the hindcast simulation results were generally in agreement with the observations except that they were underestimated at Xiamen and Dongshan, both of which were to the left of the typhoon's path, and they were also underestimated at Sansha after the typhoon landed on Taiwan Island. This may have been partly related to the topography of this area affecting the structure and strength of the typhoon low-level wind field, an effect which could not be described by the cyclone model used in this paper. The forecasted typhoon surge elevations in the early 20 h forecast period (from 0800 LST 31 August to 0400 LST 1 September) were nearly consistent with those of the hindcast results while those in the late period, after 0400 LST 1 September, were generally less accurate than the hindcast results and the measurements. Another forecast started at 0200 LST on 1 September showed that the forecasted results after 0400 LST 1 September were obviously improved, as shown in Fig. 9. This demonstrates that the storm surge predictions for typhoon Talim were better in the early 20 h forecast period of each model run than those in the late period. This is possibly because the forecasts of the typhoon track, maximum wind, and central pressure for the coming 24 h are more accurate than those for the next 48 h.

It can be seen in Fig. 9 that the computed storm surge residuals based on the analyzed data of the typhoon were a little different from the hindcast simulation results. We found that the analyzed data was also slightly different from the "best track" data. The "analyzed typhoon" from the analyzed data lagged behind the "real typhoon" from the "best track" data and was stronger. This explains the sensitivity of the model to the track, the maximum wind speed, and the central pressure of the typhoon.

The forecast experiment demonstrated that the exact predictions of the tropical cyclone track,

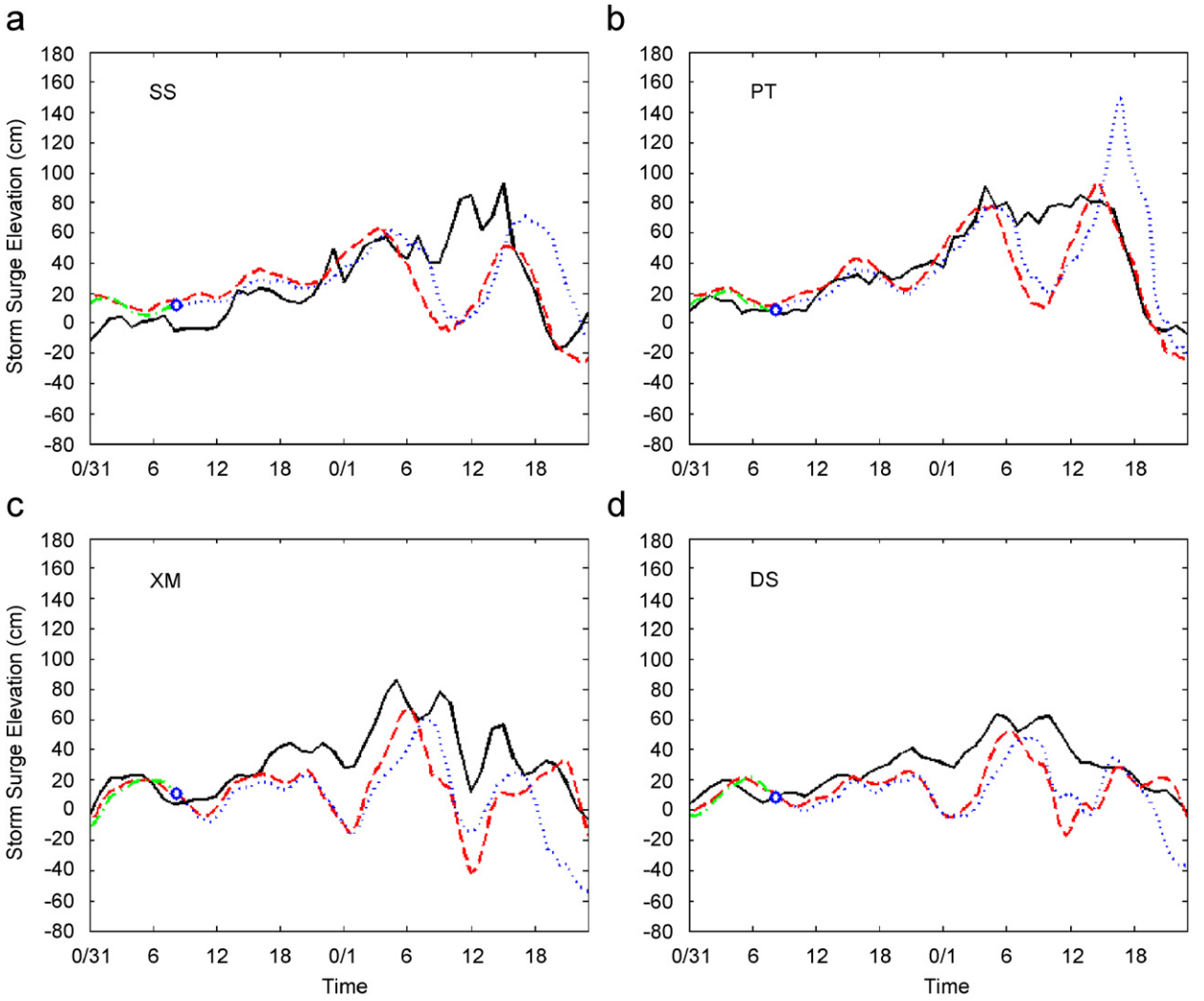

Fig. 8. Time series of measured (continuous line), hindcast simulated (broken line), calculated (dash–dotted line, based on analyzed data in real time) and forecasted (dotted line) surge residuals for the period from 0000 LST 31 August to 2300 LST 1 September 2005. Start time of the model forecast was 0800 LST 31 August, denoted by a circle.

maximum winds and central air pressures were of great importance for the model to reduce forecast errors and to improve the storm surge forecasting accuracy in this sea area. Because of this, the forecast results of storm surge residuals in the early forecast period were generally more credible than those in the late period.

Taiwan Island has a great impact on the track and the low-level wind field of tropical cyclones approaching and passing across it (Chang et al., 1993; Yeh and Elsberry, 1993; Zhang and Wu, 1996). However, the cyclone model used in this study could not describe the effect of topography on typhoon surface wind field and pressure field. Typhoon Dan was less affected by Taiwan Island than typhoon Talim, which is an important reason why the performance of storm surge hindcast simulation for Dan was better than that for Talim (see Figs. 6, 7 and 8). The calculation of the typhoon wind field in this region still needs to be improved and should take into account the effect of topography.

Another source of inaccuracy was that the error from the computation based on the analyzed typhoon data could be transferred to the later forecast, which was similar to the effect of initial conditions on the forecast. Data assimilation was not involved in this study. The assimilation process undoubtedly increases the workload of a model and requires more computing time. Under severe

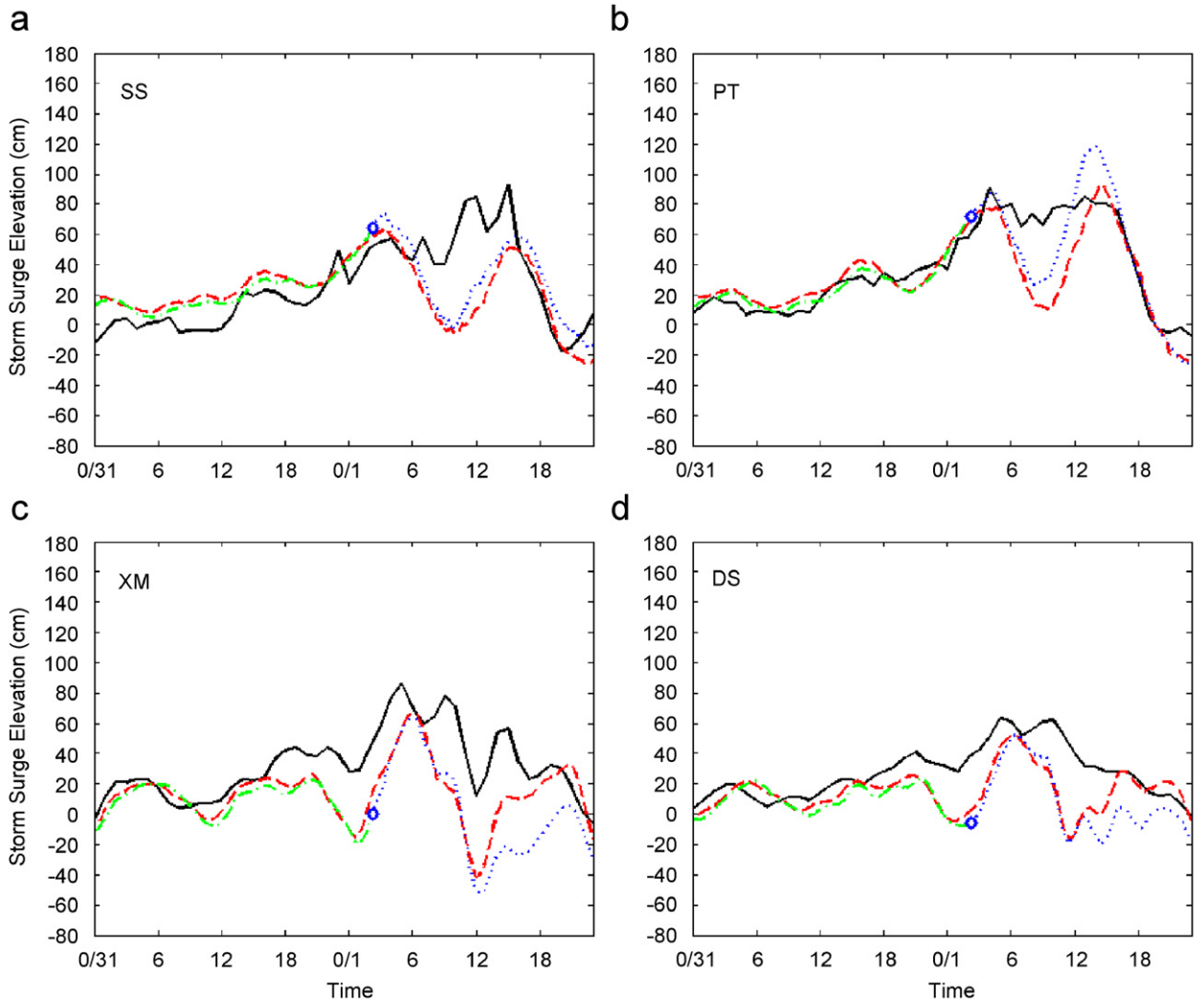

Fig. 9. Time series of measured (continuous line), hindcast simulated (broken line), calculated (dash–dotted line, based on analyzed data in real time) and forecasted (dotted line) surge residuals for the period from 0000 LST 31 August to 2300 LST 1 September 2005. Start time of the model forecast was 0200 LST 1 September, denoted by a circle.

weather and sea conditions during the lifetime of a typhoon, the available in situ data is sparse and its impact on the storm surge forecast is restricted. Although remote sensing data are plentiful, e.g. altimeter data and scatterometer wind data from satellites, currently the time intervals and delay-times to obtain these data are often too long for storm surge forecasting to be used in real time. Therefore, in view of both the prediction accuracy and the time spent in computing, at present it is uncertain whether data assimilation is advisable for operational typhoon surge forecasting.

Wave–current interaction has an evident influence on bottom stress and then on storm surge elevations in shallow coastal regions (Jones and Davies, 1998, 2001). The depth-dependent bottom friction formulation (4) reflected the general pattern of wave–current interaction effects on bottom stress in that the magnitude of bottom stress in shallow sea area is larger than that in deep-sea area. However, the present model does not really include wave–current interaction, since the accurate distribution of waves generated by a typhoon is unknown in real time. Thus, some errors due to wave–current interaction effects still remain.

The forecast experiment using NCTSM indicated that this model could be used for predicting typhoon surges in the Taiwan Strait and the adjacent sea area in real time despite the above sources of error.

4. Conclusions

A two-way nested coupled tide-surge prediction model was developed in this study and applied to the Taiwan Strait and adjacent sea area. The model had a high horizontal resolution and took into account the interaction between tides and storm surges. Thus, it is suitable for depicting the complicated physical properties of storm surges in the Taiwan Strait, where the water is quite shallow, the tidal range is very large, and the tide varies sharply. The two-way nesting technique, which makes it possible for correct information from the fine mesh to be fed back to the coarse grid mesh and, in return, more reasonable values for the open boundaries to be supplied by the coarse model to the fine model, was successfully applied in this model. It was shown that the computed results of not only the coarse model but also the fine model were improved using the two-way nesting technique in the hindcast simulations of the surges caused by typhoon Dan. Additionally, the open boundary condition used in the present model combined the radiation condition suggested by Flather (1976) and the local mode idea (Røed and Smedstad, 1984), and was slightly different from the FRO proposed by Palma and Matano (1998). In this scheme, water levels on the open boundary were specified, which took into account the function of tide input and the inverted atmospheric pressure effect. The components of current were local mode since it was impossible to predefine them exactly. However, all of the variables at the open boundary were local solutions in the FRO (Palma and Matano, 1998). The hindcast experiment for typhoon Dan and the forecast experiment for typhoon Talim confirmed that this scheme is feasible for use in the coupled tide-surge model.

Tide is of great importance in the interaction between tide and storm surge, and so we first verified the tide computation using NCTSM. The MAE of the tide computations during the period from 5 August to 20 August 2000 were smaller than 15 cm at Shansha, Pingtan, Xiamen and Dongshan. The tide computation by NCTSM was accurate enough for the storm surge forecast to take into account the coupling effect of tide and surge, although this method was not any more accurate than the harmonic method.

NCTSM was used to simulate the storm surges caused by typhoon Dan. The simulation results were in good agreement with the measurements at the Sansha, Pingtan, Xiamen and Dongshan tide gauge stations. They succeeded in reproducing the fluctuations with tidal period during the typhoon process at Sansha and Pingtan in the northern part of the Taiwan Strait. However, they were not shown by the pure storm surges, indicating that the fluctuations were not principally due to the errors of harmonically predicted tides, but were generated mainly by the interaction between tides and storm surges. This interaction produced marked differences of over 24 cm in the storm surge residuals compared to the pure storm surges at Sansha and Pingtan during the lifetime of typhoon Dan. Consequently, it would be valuable to consider the coupling effect of tides and storm surges to improve the accuracy of storm surge forecasts in a sea area such as the Taiwan Strait.

A forecast experiment was carried out in real time during the period of typhoon Talim in order to examine the forecasting capability of NCTSM. Sources of forecast errors mainly involved the three following aspects. First, the uncertainty of typhoon forecasts was a significant source of error. Secondly, the cyclone model used in this study did not take into account the effect of terrain on the wind field and the pressure field of typhoons; this could have caused a perceptible error in storm surge forecasts for some typhoons passing across Taiwan Island. Finally, the calculating error based on the analyzed typhoon data before the start time of the forecast was transferred to the surge forecast and produced a forecast error. Additionally, not including wave–current interaction may also have caused some errors due to the effects of shallow topography. These errors blended together intricately and it was too difficult to distinguish them clearly. In spite of these errors, the performance of the model in the forecast experiment was basically satisfactory. It demonstrated that NCTSM can be used by operational agencies for real-time storm surge prediction services in the Taiwan Strait.

Acknowledgements

This work was jointly supported by the China National Science Foundation grants No. 40440420596, No. 40331004 and a Special Key Project of Fujian Bureau of Science and Technology No. 2004NZ03. The authors are thankful to Professors Chen Jinquan and Hu Jianyu for their inspired discussion and to Professor Li Yan for his

valuable suggestions. The harmonic constants of tides on the open sea boundary are obtained and adjusted mainly by Ms. Zhu Jia. We thank Professor John Hodgkiss for assistance in polishing the English in this paper. We are also grateful to two anonymous reviewers for their constructive comments and helpful suggestions.

Appendix A. The numerical scheme

The numerical scheme used in the present model was developed from the Alternating Direction Implicit (ADI) scheme (Leedertse, 1967; Pan and Fang, 1995). The finite-difference grid was the staggered Arakawa "C-grid", as shown in Fig. A.1a. Time integration adopted leap-frog differencing, and the two components of depth-mean current, u and v, were computed alternately. Thus, u was computed in every half-time-step layer, v in every one-time-step layer, and ζ in every half-time-step and every one-time-step layer (shown in Fig. A.1b).

For computing the east–west component of current, u, and the corresponding water level, Eqs. (1) and (2) were approximated by

$$\frac{\zeta'^{\,n+1}_{i,j}-\zeta'^{\,n}_{i,j}}{\Delta t}+\frac{1}{R\cos\varphi_j}\left[\frac{\bar{H}^n_{+1,j}u^{n+1}_{i,j}-\bar{H}^n_{-1,j}u^{n+1}_{i-1,j}}{2\Delta\lambda}+\frac{\bar{H}^n_{+1,j}u^n_{i,j}-\bar{H}^n_{-1,j}u^n_{i-1,j}}{2\Delta\lambda}+\frac{\bar{H}^n_{i,+1}v^n_{i,j}\cos(\varphi_j+\Delta\varphi/2)-\bar{H}^n_{i,-1}v^n_{i,j-1}\cos(\varphi_j-\Delta\varphi/2)}{\Delta\varphi}\right]=0, \tag{A.1}$$

$$\frac{u^{n+1}_{i,j}-u^n_{i,j}}{\Delta t}+\frac{(u^n_{i,j}+u^n_{i+1,j})^2-(u^n_{i,j}+u^n_{i-1,j})^2}{8R\Delta\lambda\cos\varphi_j}+\frac{(v^n_{i,j}+v^n_{i+1,j})(u^n_{i,j+1}+u^n_{i,j})-(v^n_{i,j-1}+v^n_{i+1,j-1})(u^n_{i,j-1}+u^n_{i,j})}{8R\Delta\varphi}-\frac{u^n_{i,j}\bar{v}^n_{i,j}\tan\varphi_j}{R}-f\bar{v}^n_{i,j}=-\frac{g}{R\cos\varphi_j}\times\left[\frac{\zeta'^{\,n+1}_{i+1,j}-\zeta'^{\,n+1}_{i,j}}{2\Delta\lambda}+\frac{\zeta'^{\,n}_{i+1,j}-\zeta'^{\,n}_{i,j}}{2\Delta\lambda}\right]-\frac{1}{\rho R\cos\varphi_j}\times\frac{p^n_{i+1,j}-p^n_{i,j}}{\Delta\lambda}+\frac{F^n_{i,j}}{\rho\bar{H}^n_{+1,j}}-\frac{k^n_{i,j}\left[\left(u^n_{i,j}\right)^2+\left(\bar{v}^n_{i,j}\right)^2\right]^{1/2}}{\bar{H}^n_{+1,j}}u^{n+1}_{i,j}, \tag{A.2}$$

where the notations are explained as follows:

$$\zeta'^n_{i,j}=\zeta\left[i\Delta\lambda,j\Delta\varphi,\left(n-\tfrac{1}{2}\right)\Delta t\right],$$

$$\zeta^n_{i,j}=\zeta[i\Delta\lambda,j\Delta\varphi,n\Delta t],$$

$$u^n_{i,j}=u\left[\left(i+\tfrac{1}{2}\right)\Delta\lambda,j\Delta\varphi,\left(n-\tfrac{1}{2}\right)\Delta t\right],$$

$$v^n_{i,j}=v\left[i\Delta\lambda,\left(j+\tfrac{1}{2}\right)\Delta\varphi,n\Delta t\right],$$

$$\bar{v}^n_{i,j}=\tfrac{1}{4}\left(v^n_{i,j-1}+v^n_{i,j}+v^n_{i+1,j-1}+v^n_{i+1,j}\right),$$

$$h_{i,j}=h[i\Delta x,j\Delta y],$$

$$\bar{H}^n_{-1,j}=\tfrac{1}{2}\left(h_{i-1,j}+\zeta^n_{i-1,j}+h_{i,j}+\zeta^n_{i,j}\right),$$

$$\bar{H}^n_{+1,j}=\tfrac{1}{2}\left(h_{i,j}+\zeta^n_{i,j}+h_{i+1,j}+\zeta^n_{i+1,j}\right),$$

$$\bar{H}^n_{i,-1}=\tfrac{1}{2}\left(h_{i,j-1}+\zeta^n_{i,j-1}+h_{i,j}+\zeta^n_{i,j}\right),$$

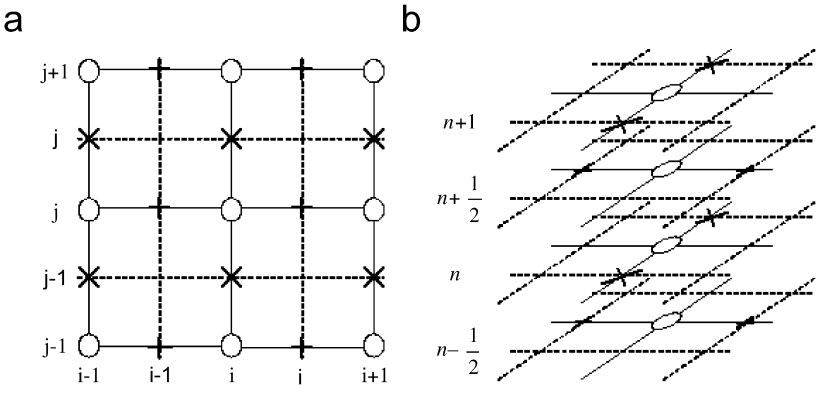

Fig. A.1. Finite-difference grid: (a) spatial distribution of grid points and (b) temporal calculation order of grid points.

$$\bar{H}^n_{i,+1} = \tfrac{1}{2}\left(h_{i,j} + \zeta^n_{i,j} + h_{i,j+1} + \zeta^n_{i,j+1}\right),$$

$$p^n_{i,j} = p_a[i\Delta\lambda, j\Delta\varphi, n\Delta t],$$

$$F^n_{i,j} = F_s\left[\left(i+\tfrac{1}{2}\right)\Delta\lambda, j\Delta\varphi, n\Delta t\right],$$

$$k^n_{i,j} = gc^{-2} = gn^2\left(\bar{H}^n_{+1,j}\right)^{-1/3}.$$

Δt is the time step and n the time-step number. $\Delta\lambda$ and $\Delta\varphi$ are the east-west and the south-north grid spacing, respectively. The point number in longitude, i, increases from west to east and in latitude, j, increases from south to north. φ_j is the latitude of the jth row. For the sake of the leap-frog difference in time, in the first step, u and ζ' are integrated for a half step by forward time differencing.

A similar approach was used for the south-north currents and elevations.

Based on Eqs. (8)–(10) and the local solutions, the open boundary conditions could be obtained. For example, the open boundary condition on the eastern side was as follows:

$$u^{n+1}_{b-1,j} = \widehat{u}^{n+1}_{b-1,j} + \sqrt{\frac{g}{\bar{H}^n_{-1,j}}}\left(\zeta'^{\,n+1}_{b,j} - \widehat{\zeta}'^{n+1}_{b,j}\right), \tag{A.3}$$

where the subscript b denotes the point at the open boundary of the larger domain and $\widehat{\zeta}'$ is the input of water level, composing of tide and contribution due to the inverted pressure effect. $\widehat{u}$ is the local mode of u, following Røed and Smedstad (1984), and is calculated by the corresponding difference form of Eq. (11):

$$\frac{u^{n+1}_{b-1,j} - u^n_{b-1,j}}{\Delta t} = \frac{u^n_{b-1,j}\bar{v}^n_{b-1,j}\tan\varphi_j}{R} + f\bar{v}^n_{b-1,j} + \frac{F^n_{b-1,j}}{\rho\bar{H}^n_{+1,j}} - \frac{k^n_{b-1,j}\left[\left(u^n_{b-1,j}\right)^2 + \left(\bar{v}^n_{b-1,j}\right)^2\right]^{1/2}}{\bar{H}^n_{+1,j}}\,u^{n+1}_{b-1,j}. \tag{A.4}$$

v on the eastern open boundary is directly calculated by the corresponding difference forms of Eqs. (12) and (13) as follows:

$$\frac{v^{n+1}_{b,j} - v^n_{b,j}}{\Delta t} = -\frac{\left(\bar{u}^{n+1}_{b,j}\right)^2\tan\left(\varphi_j + \Delta\varphi/2\right)}{R} - f\bar{u}^{n+1}_{b,j} - \frac{g}{R}\left[\frac{\zeta^{n+1}_{b,j+1} - \zeta^{n+1}_{b,j}}{2\Delta\varphi} + \frac{\zeta^n_{b,j+1} - \zeta^n_{b,j}}{2\Delta\varphi}\right] - \frac{1}{\rho R}\frac{p'^{n+1}_{b,j+1} - p'^{n+1}_{b,j}}{\Delta\varphi} + \frac{G^n_{b,j}}{\rho\bar{H}'^{\,n+1}_{b,+1}} - \frac{k'^{\,n+1}_{b,j}\left[\left(\bar{u}^{n+1}_{b,j}\right)^2 + \left(v^n_{b,j}\right)^2\right]^{1/2}}{\bar{H}'^{n+1}_{b,+1}}\,v^{n+1}_{b,j}, \tag{A.5}$$

$$\frac{\zeta^{n+1}_{b,j} - \zeta^n_{b,j}}{\Delta t} = \frac{\bar{H}'^{n+1}_{b,-1}v^{n+1}_{b,j-1}\cos\left(\varphi_j - \Delta\varphi/2\right) - \bar{H}'^{n+1}_{b,+1}v^{n+1}_{b,j}\cos(\varphi_j + \Delta\varphi/2)}{2R\cos\varphi_j\Delta\varphi} + \frac{\bar{H}'^{n+1}_{b,-1}v^n_{b,j-1}\cos\left(\varphi_j - \Delta\varphi/2\right) - \bar{H}'^{n+1}_{b,+1}v^n_{b,j}\cos\left(\varphi_j + \Delta\varphi/2\right)}{2R\cos\varphi_j\Delta\varphi}, \tag{A.6}$$

where

$$\bar{u}^{n+1}_{b,j} = \tfrac{1}{4}\left(u^{n+1}_{b-1,j} + u^{n+1}_{b,j} + u^{n+1}_{b-1,j+1} + u^{n+1}_{b,j+1}\right),$$

$$p'^{n+1}_{b,j} = p_a\left[b\Delta\lambda, j\Delta\varphi, \left(n+\tfrac{1}{2}\right)\Delta t\right],$$

$$G^n_{b,j} = G_s\left[b\Delta\lambda, \left(j+\tfrac{1}{2}\right)\Delta\varphi, \left(n+\tfrac{1}{2}\right)\Delta t\right],$$

$$\bar{H}'^{\,n+1}_{b,-1} = \tfrac{1}{2}\left(h_{b,j-1} + \zeta'^{\,n+1}_{b,j-1} + h_{b,j} + \zeta'^{\,n+1}_{b,j}\right),$$

$$\bar{H}'^{n+1}_{b,+1} = \tfrac{1}{2}\left(h_{b,j+1} + \zeta'^{n+1}_{b,j+1} + h_{b,j} + \zeta'^{n+1}_{b,j}\right),$$

$$k'^{\,n+1}_{b,j} = gc^{-2} = gn^2\left(\bar{H}'^{n+1}_{b,+1}\right)^{-1/3}.$$

Because two of the four points used for computing $\bar{u}^{n+1}_{b,j}$ are not inside the domain, $\bar{u}^{n+1}_{b,j}$ in Eq. (A.5) was approximately by

$$\bar{u}^{n+1}_{b,j} = \left(u^{n+1}_{b-1,j} + u^{n+1}_{b-1,j+1}\right)/2. \tag{A.7}$$

The open boundary condition at the eastern side of the fine mesh domain is similar to Eq. (A.3). However, here $\widehat{\zeta}'$ at the eastern open boundary of the fine mesh domain is directly interpolated from the coarse mesh, and $\widehat{u}$ and v are obtained through the mass flux interpolated from the coarse mesh with the cubic spline method.

Eqs. (A.1) and (A.2) with corresponding open boundary conditions can be resolved row by row (column by column for the counterparts in the south–north direction) in the whole domain, using the double sweeping method or the Gauss method. Avoiding the artificial vibration due to the leap-frog differencing, the values of ζ and ζ' at each time step are slightly smoothed, respectively, as

follows:

$$\zeta_{i,j}^{n}\Big|_{new} = (1-\varepsilon)\zeta_{i,j}^{n}\Big|_{old} + \frac{\varepsilon}{2}\left(\zeta_{i,j}'^{\,n} + \zeta_{i,j}'^{\,n+1}\right), \tag{A.8}$$

$$\zeta_{i,j}'^{\,n+1}\Big|_{new} = (1-\varepsilon)\zeta_{i,j}'^{\,n+1}\Big|_{old} + \frac{\varepsilon}{2}\left(\zeta_{i,j}^{n} + \zeta_{i,j}^{n+1}\right), \tag{A.9}$$

where ε is a small value between 0 and 0.5 that can be determined by experience and 0.06 is adopted in this study.

References

Ådlandsvik, B., Hansen, R., 1998. Numerical simulation of the circulation in the Svalbardbanken area in the Barents Sea. Continental Shelf Research 18, 341–355.

Atkinson, G.D., Holliday, C.R., 1977. Tropical cyclone minimum sea level pressure/maximum sustained wind relationship for the western North Pacific. Monthly Weather Review 105, 421–427.

Bao, X., Gao, G., Yan, J., 2001. Three dimensional simulation of tide and tidal current characteristics in the East China Sea. Oceanologica Acta 24 (2), 135–149.

Chang, C.-P., Yeh, T.-C., Chen, J.M., 1993. Effects of terrain on the surface structure of typhoons over Taiwan. Monthly Weather Review 121, 734–752.

Chen, J.Q., Shang, S.P., Lin, K., Zhang, H.J., 1990. A two-dimensional numerical model for predicting total water elevation in tidal rivers or bays. In: Proceedings of the 1987 International Symposium on Storm Surge. China Ocean Press, Beijing, China, pp. 163–172.

Davies, A.M., Flather, R.A., 1978. Application of numerical models of the North West European continental shelf and the North Sea to the computation of the storm surges of November to December 1973. Deutsche Hydrographische Zeitschrift Ergänzungsheft Reihe A, No. 14, 72pp.

Davies, A.M., Kwong, S.C.M., Flather, R.A., 2000. On determining the role of wind wave turbulence and grid resolution upon computed storm driven currents. Continental Shelf Research 20 (14), 1825–1888.

Fang, G., Yang, J., Zhao, X., 1985. A numerical model for the tides and tidal currents in the Taiwan Strait. Acta Oceanologica Sinica 4 (2), 189–200.

Flather, R.A., 1976. A tidal model of the north-west European continental shelf. Mémoires Société Royale des Sciences de Liège 6 (10), 141–164.

Flather, R.A., 1994. A storm surge prediction model for the northern Bay of Bengal with application to the cyclone disaster in April 1991. Journal of Physical Oceanography 24, 172–190.

Flather, R.A., 2000. Existing operational oceanography. Coastal Engineering 41, 13–40.

Foreman, M.G.G., 1977. Manual for tidal heights analysis and prediction (revised in 2004). Pacific Marine Science Report 77-10, Institute of Ocean Sciences, Patrica Bay, Victoria, B.C., Canada.

Garratt, J.R., 1977. Review of drag coefficients over oceans and continents. Monthly Weather Review 105, 915–929.

Geernaert, G.L., Larsen, S.E., Hansen, F., 1987. Measurements of the wind stress, heat flux, and turbulence intensity during storm conditions over the North Sea. Journal of Geophysical Research 92 (C12), 13127–13139.

Holland, G.J., 1980. An analytic model of the wind and pressure profiles in hurricanes. Monthly Weather Review 108, 1212–1218.

Hu, F.X., Gu, G.C., 1989. Seasonal changes of the mean tidal range along the Chinese coasts. Oceanologia et Limnologia Sinica 20 (5), 401–411 (in Chinese, English abstract).

Jakobsen, F., Madsen, H., 2004. Comparison and further development of parametric tropical cyclone models for storm surge modelling. Journal of Wind Engineering and Industrial Aerodynamics 92, 375–391.

Jelesnianski, C.P., 1965. A numerical calculation of storm tides induced by a tropical storm impinging on a continental shelf. Monthly Weather Review 93 (6), 343–358.

Jones, J.E., Davies, A.M., 1998. Storm surge computations for the Irish Sea using a three-dimensional numerical model including wave–current interaction. Continental Shelf Research 18, 201–251.

Jones, J.E., Davies, A.M., 2001. Influence of wave–current interaction, and high frequency forcing upon storm induced currents and elevations. Estuarine, Coastal and Shelf Science 53 (4), 397–413.

Kang, S.K., Lee, S.R., Lie, H.J., 1998. Fine grid tidal modeling of the Yellow and East China Seas. Continental Shelf Research 18, 739–772.

Koch, S.E., McQueen, J.T., 1987. A survey of nested grid techniques and their potential for use within the MASS weather prediction model. NASA Technical Memorandum 87808, National Aeronautics and Space Administration, USA.

Kunz, R., Moussiopoulos, N., 1997. Implementation and assessment of a one-way nesting technique for high resolution wind flow simulations. Atmospheric Environment 31 (19), 3167–3176.

Large, W.G., Pond, S., 1981. Open ocean momentum flux measurements in moderate to strong winds. Journal of Physical Oceanography 11, 324–336.

Leedertse, J.J., 1967. Aspects of a computational model for long period water-wave propagation. Rep. RM-5294-PR. Rand Cooperation, Santa Monica, CA, 165 pp.

Li, Y.C., Cai, W.L., Li, L., Lin, M.S., 2002. The tide characteristics of the seas adjacent to Fujian and Taiwan derived from TOPEX/POSEIDON altimeter data. Acta Oceanologica Sinica 24 (1), 154–162 (in Chinese, English abstract).

Matsumoto, K., Takanezawa, T., Ooe, M., 2000. Ocean tide models developed by assimilating TOPEX/POSEIDON altimeter data into hydrodynamical model: a global model and a regional model around Japan. Journal of Oceanography 56, 567–581.

Monbaliu, J., Padilla-Hernández, R., Hargreaves, J.C., Carretero Albiach, J.C., Luo, W., Sclavo, M., Günther, H., 2000. The spectral wave model, WAM, adapted for applications with high spatial resolution. Coastal Engineering 41, 41–62.

Palma, E.D., Matano, R.P., 1998. On the implementation of passive open boundary conditions for a general circulation model: the barotropic mode. Journal of Geophysical Research 103 (C1), 1319–1341.

Pan, H., Liu, F.S., 1994. A numerical study of the tide-surge interaction in the East China Sea and the South China Sea. Chinese Journal of Oceanology and Limnology 12 (1), 13–21.

Pan, H., Fang, G., 1995. A two-dimensional alternating direction implicit model for ocean hydrodynamics. Acta Oceanologica Sinica 17 (5), 21–31 (in Chinese).

Powell, M.D., Vickery, P.J., Reinhold, T.A., 2003. Reduced drag coefficient for high wind speeds in tropical cyclones. Nature 422, 279–283.

Prandle, D., Wolf, J., 1978. Surge-tide interaction in the southern North Sea. In: Proceedings of the Ninth International Liege Colloqium on Ocean Hydrodynamics. Elservier, Amsterdam, The Netherlands, pp. 161–185.

Røed, L.P., Smedstad, O.M., 1984. Open boundary conditions for forced waves in a rotating fluid. SIAM Journal on Scientific Computing 5 (2), 414–426.

Roy, G.D., 1995. Estimation of expected maximum possible water level along the Meghna Estuary using a tide and surge interaction model. Environment International 21 (5), 671–677.

Smith, S.D., 1980. Wind stress and heat flux over the ocean in gale force winds. Journal of Physical Oceanography 10, 709–726.

Sun, W.X., Luo, Y.Y., Wang, J.Y., 1994. Numerical modelling of storm surges in the Beibu Gulf with SCM. Acta Oceanologica Sinica 13 (4), 475–483.

Wang, X.N., Yin, Q.J., Zhang, B.M., 1991. Research and applications of a forecasting model of typhoon surges in China seas. Advances in Water Science 2 (1), 1–10 (in Chinese, English abstract).

Wu, J., 1982. Wind-stress coefficients over sea surface from breeze to hurricane. Journal of Geophysical Research 87, 9704–9706.

Wu, P.M., 1984. A numerical prediction model for typhoon surge along the southeast coast of China. Acta Oceanologica Sinica 3 (1), 45–55.

Wu, P.M., Xu, Y.S., Li, Y.C., Chen, Y.X., Chen, J.L., 1982. Nonlinear numerical computations on storm surges of the Taiwan Strait. Acta Oceanologica Sinica 1 (2), 195–203.

Ye, A.L., Chen, Z.Y., Yu, Y.F., 1985. Numerical investigation of three-dimensional semidiurnal tidal waves in Taiwan Strait and its adjacent areas. Oceanologia et Limnologia Sinica 16 (6), 439–450 (in Chinese, English abstract).

Yeh, T.-C., Elsberry, R.L., 1993. Interaction of typhoons with the Taiwan Orography. Part I: upstream track deflections. Monthly Weather Review 121, 3193–3212.

Yelland, M., Taylor, P.K., 1996. Wind stress measurements from the open ocean. Journal of Physical Oceanography 26, 541–558.

Yu, F.J., Zhang, Z.H., 2002. Implementation and application of a nested numerical storm surge forecast model in the East China Sea. Acta Oceanologica Sinica 21 (1), 19–31.

Zhang, M.Y., Li, Y.S., 1996. The synchronous coupling of a third-generation wave model and a two-dimensional storm surge model. Ocean Engineering 23 (6), 533–543.

Zhang, M.Y., Li, Y.S., 1997. The dynamic coupling of a third-generation wave model and a 3D hydrodynamic model through boundary layers. Continental Shelf Research 17 (10), 1141–1170.

Zhang, W.Z., Wu, Z.M., 1996. Analyses of the effects of the Taiwan Island on typhoon tracks. Marine Forecasts 13 (4), 31–38 (in Chinese, English abstract).

Zhang, W.Z., Hu, J.Y., Shang, S.P., Chen, M.N., She, W.M., 2004. On the characteristics of storm surges along Fujian coast. Marine Science Bulletin 23 (3), 12–19 (in Chinese, English abstract).

Zhang, Y.T., Wang, Y.J., 1990. Numerical simulations of coupling effects between storm surge and astronomical tide, sea level and current fields in the Bohai Sea. In: Proceedings of the 1987 International Symposium on Storm Surge. China Ocean Press, Beijing, China, pp. 71–81.

Zhen, W.Z., Chen, F.N., Chen, X.Z., 1982. Tides and tidal currents in the Taiwan Strait. Taiwan Strait 1 (2), 1–4 (in Chinese, English abstract).